Temporal Characterization of VR Traffic for Network Slicing Requirement Definition

Federico Chiariotti, *Member, IEEE,* Matteo Drago, *Student Member, IEEE,*
Paolo Testolina, *Student Member, IEEE,* Mattia Lecci, *Student Member, IEEE,*
Andrea Zanella, *Senior Member, IEEE,* and Michele Zorzi, *Fellow, IEEE*

Abstract—Over the past few years, the concept of VR has attracted increasing interest thanks to its extensive industrial and commercial applications. Currently, the 3D models of the virtual scenes are generally stored in the VR visor itself, which operates as a standalone device. However, applications that entail multi-party interactions will likely require the scene to be processed by an external server and then streamed to the visors. However, the stringent Quality of Service (QoS) constraints imposed by VR's interactive nature require Network Slicing (NS) solutions, for which profiling the traffic generated by the VR application is crucial. To this end, we collected more than 4 hours of traces in a real setup and analyzed their temporal correlation. More specifically, we focused on the CBR encoding mode, which should generate more predictable traffic streams. From the collected data, we then distilled two prediction models for future frame size, which can be instrumental in the design of dynamic resource allocation algorithms. Our results show that even the state-of-the-art H.264 CBR mode can have significant fluctuations, which can impact the NS optimization. We then exploited the proposed models to dynamically determine the Service Level Agreement (SLA) parameters in an NS scenario, providing service with the required QoS while minimizing resource usage.

Index Terms—Virtual Reality, Extended Reality, Traffic Modeling, Network Slicing, Resource Provisioning

✦

1 INTRODUCTION

OVER the past few years, the rapid technological development of Head Mounted Devices (HMDs) and the strong push towards the virtual world caused by the COVID-19 pandemic led to an explosion of the eXtended Reality (XR) market, which includes technologies such as Virtual Reality (VR), Augmented Reality (AR), and Mixed Reality (MR). Recent studies estimate hundreds of millions of users of these technologies in a time span of just 3 years [1], requiring millions of new devices to be developed, produced, and shipped around the world for a business in the order of billions of dollars [2].

While the latest news on the *metaverse* seem to indicate that the fastest growth will be in the entertainment and social media industries, XR is expected to make an impact in a wide variety of scenarios [3], [4]. Interactive design, marketing, healthcare, and employee training are just a few of the proposed use cases, but industrial remote control in manufacturing and agriculture might have the largest impact, allowing human operators to remotely control machines in risky, hard to reach or unsafe environments, through a fully interactive virtual framework.

A common characteristic of all these new applications is their interactive nature: users do not passively receive the information or stream a video, but need to manipulate the environment while maintaining an illusion of presence that requires the application to operate under very strict end-to-end delay constraints [5], [6]. In particular, safety-critical and industrial applications will have even stricter constraints, as the consequences of network impairments can be significantly more serious. *Cybersickness* is another important issue, as a delay over 20 ms between movements and visual and auditory feedback can cause disorientation and dizziness [1], [7].

In order to fulfill these stringent latency requirements over a wireless connection, the application and the network need to cooperate. The *Network Slicing (NS)* paradigm [8] allows 5G and Beyond networks to reserve resources to a given stream, defining Quality of Service (QoS) targets. Most works in this area, however, focus on relatively predictable applications. In this setting, the need for predictability in the XR traffic becomes extremely important, leading to a resurgence of *quasi*-Constant Bit Rate (CBR) encoders, which are not used in non-interactive streaming due to their lower picture quality stability. While some efforts have been devoted by prominent standard bodies on this topic [5], [6], the current availability of traffic models for XR is scarce. Furthermore, to the best of our knowledge, no detailed analysis of the temporal statistics of *quasi*-CBR video streams can be found in the literature, making existing slicing schemes rely on uncertain foundations. This makes the definition of a Service Level Agreement (SLA) for XR traffic more complex: most NS solutions assume that each application's demand in terms of required throughput and latency is known, but such a characterization can be difficult in case

of streams with variable frame size, requiring significant overprovisioning.

However, even CBR encoders are not perfect, and the interplay between the video content and the movements and actions of the users may cause significant fluctuations. In this work, we analyze the traffic from a real VR application using the *Periodic-Intra Refresh* mode of the H.264 codec, which results in relatively small differences in the frame sizes. Modeling these imperfections, and consequently predicting the size of future frames in advance, can be extremely significant in the allocation of network resources, particularly if some critical QoS metrics have to be reached. For example, this is the case for *Cloud XR*, a new trend pursued by some major players in the telecommunications industry that moves the processing and rendering steps of the XR content from the user to the Cloud, making the QoS requirements even more critical [9], [10]. This increases the need for a dynamic SLA that can allow an NS system to provide low-latency service to XR applications without wasting too many resources: as we mentioned above, a static definition of the required throughput would require significant overprovisioning, while a temporal model of the XR traffic stream could allow to predict the future needs of the application, tailoring the QoS requirements in the SLA to what will actually be needed.

Hence, in this paper we address the problem of providing a realistic stochastic characterization of a VR traffic source, so as to allow for a dynamic provisioning of bandwidth resources for VR users to satisfy the latency constraints. Our analysis can also be applied to the downlink part of generic XR traffic.

Building upon our previous works [11], [12], in which we collected more than 4 hours of live sessions and performed basic traffic characterization, in this paper we take the analysis one step further by modeling the size of VR frames in the stream as a correlated time series that is then used to derive an adaptive and predictive SLA. The contributions of this paper are the following:

- We propose two parametric regression models to predict the size of future frames, and show that these models can be generalized to other traces and even different applications with limited regression performance loss;
- We analyze the residual error of these predictors, providing a full statistical model of future frame sizes;
- We show that the prediction can be successfully used for efficient resource allocation in an NS scenario;
- We consider different NS modes, including per-user or application-level slicing, and compare the performance of different schemes in terms of the trade-off between resource utilization and latency.

A partial version of this work was presented in [13]. This work significantly extends it by exploring the statistical analysis of frame sizes at a deeper level, including the characterization of the residual error of the predictors, and expanding on the SLA definition, including the use case with multiple VR users. All our traces, as well as the analysis and simulation code, are publicly available.[1]

The rest of the paper is structured as follows. Sec. 2 will discuss the current state of the art on XR modeling, and our experimental setup is briefly presented in Sec. 3. Our analysis is reported in Sec. 4, while Sec. 5 illustrates how our analysis can be leveraged for a simple NS use case by designing predictive resource allocation mechanisms and testing their performance in a simple simulation scenario. Finally, Sec. 7 draws conclusions and presents some avenues for future work.

2 STATE OF THE ART

Despite a steady scientific interest in VR since the 1990s [14], relatively little work has been done to characterize the details of this type of traffic. We can distinguish four main areas of research: the reduction of the Motion-To-Photon (MTP) latency, the modeling and characterization of XR traffic, the use of traffic models in NS, and the scheduling and resource management of XR data streams.

2.1 Motion-To-Photon latency and VR sickness

The MTP latency is defined as the time difference between the beginning of a movement of the user's head and the instant when the image that corresponds to the user motion is shown on the HMD screen. This phenomenon is one of the main factors causing sickness when experiencing XR content, the main symptoms being discomfort, nausea, cold sweating, eye fatigue, and disorientation.

From a research point of view, a lot of effort has been devoted to avoiding such episodes in the first place, and the IEEE issued a dedicated standard in 2021 [15], which addressed the content design, sickness assessment and measurement, and the network requirements that may influence the MTP latency as the three main areas to consider in order to reduce or control bad user experience.

First of all, measuring the MTP latency represents a challenge *per se*. The architecture described in [16], which consists of a control PC, a head position model-based rotary platform, a pixel luminance change detector which converts the change in the display into a voltage value, and a digital oscilloscope to show such voltage information, is used as reference in [15]. Specifically, after a movement of the rotary platform is generated by the control PC, the MTP latency is measured as the time difference between the platform's movement and the corresponding change of the voltage value given by the oscilloscope.

To obtain a robust estimate of the MTP latency, a precise head tracking algorithm is of the utmost importance. The authors of [17] presented a 6 Degrees of Freedom (6DoF), optical head tracking instrument with a declared motion-to-pose latency (i.e., the time between a change in the users pose and the tracker actually detecting the movement) of about 28 μs, at a sample rate of 50 kHz. In their work, they also showed that the difference between the tracker's pose output and the user's true pose is proportional to pose velocity, tracker sampling rate, tracking latency, and noise. Moreover, the authors of [18] showed that latency jitter

---

1. Code repository: https://github.com/signetlabdei/vr-trace-analysis

artifacts already occur with a low system load by injecting artificial latency in a VR simulation. Even though their hypothesis included the tracking algorithm of the specific HMD as the possible cause of such jitter spikes, they did not prove it empirically.

Both rotational and translational MTP latencies were estimated in [19] by calculating the phase shift between the captured signals of the physical motion of the HMD and a motion-dependent gradient stimulus rendered on the display. They were able to conclude that rapid head movements may elicit stronger disorientation to users in VR environments than slower head movements do. Even though the measurements were carried out with an Oculus Rift DK2, the proposed methodology is general and can be applied to other HMDs as well. The authors of [20] also measured the MTP latency with different workloads (determined by the complexity of the scene to render), finding that it can span from a minimum of 45 ms to a maximum of 155 ms. In general, the network requirements defined by the standard [15] are way more stringent: approximately 5 ms for the wireless transmission and 20 ms in total for the MTP latency, with a jitter strictly lower than 5 ms.

2.2 XR Traffic Characterization

XR traffic modeling is closely related to 2D video content, and, even more so, to live, interactive applications such as video conferencing and gaming. However, most of the work on the subject has considered the customary encoding schemes for pre-recorded video streaming, i.e., the Variable Bit Rate (VBR) encoding based on either the H.264 or the H.265 standard [21]. VBR can provide a stable visual quality, improving the user's Quality of Experience (QoE), but is also subject to significant jitter due to the large frame size fluctuations. Transmitting VBR videos with low latency can then be a significant challenge even over channels with constant capacity [22]. On the other hand, CBR encoding sacrifices some visual quality stability to obtain an encoded video stream with a stable transmission rate [23]. Although the higher predictability of the encoded output makes CBR encoding attractive for interactive video and XR content, it is still relatively unexplored in the relevant literature.

A topic related to XR traffic is video game streaming, also called *Cloud gaming*. Games run on remote servers and the scenes are streamed directly to the users without the need for client-side computation. The stringent requirements of gaming applications, especially in terms of latency, and the need to address them with optimized protocols and new transmission strategies, have led to an increased interest in their characterization.

The authors of [24] carried out an extensive measurement campaign in Google Stadia, a popular Cloud gaming platform, giving an overview of its inner working. They studied the distributions of downlink traffic, packet size and inter-packet time under multiple settings, including different resolutions, video codecs, and network conditions. On the other hand, in [25], [26] direct comparisons were made between different Cloud gaming platforms, mostly focusing only on the bit rate of the video stream, without including latencies or user experience.

A more comprehensive Cloud gaming testbed, including automated trace acquisition over Ethernet, WiFi, and LTE,

was presented in [27]. Automating the acquisitions surely gives an advantage in terms of reproducibility and speed of the experiments, but the unpredictability of the users' actions in gaming scenarios (and, more importantly, in XR) is the real challenge that the network has to face, limiting the usefulness of the results. These works represent a good starting point for the collection and modeling of VR traffic, as it is reasonable to assume that most of these Cloud gaming companies will start providing VR services soon. However, most works still focused on simple applications, such as interactive data visualization [28], and do not provide much insight on more complex scenarios. There is an extensive literature on immersive video streaming [29], but it has been mostly focused on passive applications in which the user is only a viewer, with different QoE and encoding considerations. A recent document by the 3GPP [30] also provided a simple model for XR traffic, which however does not consider temporal or video content aspects, and is thus usable for general feasibility studies, but not for fine-grained optimization.

2.3 Prediction-Based Slicing

The use of traffic prediction in NS is a concept that was first explored in [31]: as slicing requires precise SLAs to provide QoS to different services, but most practical applications are VBR, characterizing the traffic and predicting future requests is a way to allocate resources in a foresighted manner, performing resource allocation on a short timescale and admission control on a longer one. If we consider wider networks with massive numbers of users, the daily, weekly, and seasonal cycles of network usage can also be exploited to allocate resources more effectively [32]. This work, however, will focus on shorter-term predictions over a limited number of XR flows. Other works such as [33] have also explored the possibility of exploiting longer-term trends for a rough resource allocation, while using a short-term scheduler for fine-grained optimization.

In particular, the use of Auto-Regressive Moving Average (ARMA) models has been explored in [34] as a potential application-agnostic prediction method to perform resource allocation: as the orchestrator knows the state of the packet buffer for each slice, it can perform the moving average and allocate resources accordingly. However, ARMA models require a certain number of past samples, and this approach cannot discriminate between different applications: consequently, the initial performance will be lower when compared to an application-aware model that takes knowledge of the traffic source into account. In order to capture the behavior of more complex traffic sources, it is also possible to replace the ARMA model with a Long Short-Term Memory (LSTM) deep neural network [35], which can generalize to non-linear and longer-term patterns. Deep reinforcement learning [36] is another alternative, as it can implicitly learn even complex application behaviors and take them into account when slicing.

Another recent idea is to combine NS with video bit rate adaptation: if we consider QoE as a flexible metric over which we can compromise in high traffic conditions, a cross-layer approach allows the orchestrator to dictate the video bit rate for the next few frames [37], limiting the demands

of the interactive video flow to what the network is able to support. This approach is complementary to the prediction-based one, as these bit rate changes need to be relatively infrequent to avoid annoying the user, and such a system would operate over a longer timescale: while the prediction and allocation of resources is usually performed over tens or hundreds of milliseconds, video bit rate adaptation spans multiple seconds, and the two approaches can be integrated.

2.4 XR Resource Management

Although the management of XR flows is a relatively new problem, a few works have already discussed efficient schemes for providing QoS to these applications. For example, in [38], [39] game-theoretic approaches are proposed to tackle the optimization of multi-user VR streaming over a small cell, with the help of machine learning. The authors of [40] analyze the scheduling problem from the perspective of Mobile Edge Cloud (MEC), proposing scheduling strategies and analyzing communication, computing, and caching trade-offs. While the models proposed for the network architectures considered in these works are extremely complex, there is no comparison with real-world VR streaming.

To the best of our knowledge, our previous works, which proposed a simple architecture for collecting traffic traces from VR games [11] and a simple generative model for the frame size [12], were the first to use real VR traffic traces. This paper extends our previous works by characterizing the temporal behavior of the VR traces and drawing novel conclusions for NS optimization.

3 VR STREAMING ARCHITECTURE

In this section, we describe the architecture of our VR streaming acquisition and give some perspective on the full end-to-end setup. To further understand what are the steps that most influence the VR performance, it is useful to describe a common end-to-end VR architecture. First, we can start from the collection and processing of tracking information, delegated to the HMD. Then, this information is sent to a remote server to compose the viewport, i.e., what is actually shown to the user. This process includes the rendering of the scene, the video encoding providing a more robust transmission towards the mobile device, and possibly some additional information, e.g., the direction in which the rendered frame is supposed to be displayed. After receiving and decoding the video stream together with all the additional meta-information, the HMD generates the images to display at the occurring screen refresh rate. These steps need to be accomplished with minimal delay to guarantee adequate QoE.

Our experimental setup consisted of a desktop computer equipped with an NVIDIA GeForce RTX 2080 Ti graphics card acting as the rendering server, and an iPhone XS enclosed in a VR cardboard acting as the HMD. VR applications were thus run on the rendering server and streamed to the headset using the *RiftCat 2.0* application (on the server), and *VRidge* 2.7.7 (on the phone).[2]

The application uses hardware-accelerated H.264 encoding via Nvidia Encoder (NVENC) as long as a compatible

2. https://riftcat.com/vridge

graphics card is available to the system. *RiftCat*'s developers disclosed that Periodic Intra-Refresh is used, a setting provided by the encoder that allows each frame to be roughly the same size, making the stream almost CBR and thus easier to handle from a network perspective. It does so by replacing key frames with *waves* of refreshed intra-coded blocks, i.e., blocks without any dependence on other frames, effectively spreading a key frame over multiple frames. Image quality is balanced with resilience to packet loss by setting the `intraRefreshPeriod`, a parameter that determines the period after which an intra refresh happens again, and the `intraRefreshCnt` parameter, which sets the number of frames over which the intra refresh happens [41]. If we consider a 30 Frames per Second (FPS) video, a value of 30 for the `intraRefreshPeriod` would ensure that the frame is fully recovered every second. On the other hand, choosing small values of `intraRefreshCnt` leads to a quicker refresh but lower quality.

Detailed information about the video encoder is fundamental for our work, since different encoders typically behave differently, especially when analyzing the temporal behavior of the encoded source. Still, we believe that our work offers network researchers a peek into the intricacies of this topic, showing some key results on how a VR traffic flow can be analyzed for resource provisioning.

Different freely available games and applications were used to acquire our dataset, including *Minecraft*, *Virus Popper*, and *Google Earth VR*. Further details on the acquisition setup and our traces can be found in [12]. In the following, we will mostly concentrate on one trace acquired using the *Virus Popper* application, but the methodology holds throughout the dataset, and can be easily replicated for any of the other traces.

4 VIDEO TRACE ANALYSIS

By analyzing the acquired traces, we determined that the application used User Datagram Protocol (UDP) over IPv4. It also used an additional application-layer protocol header of variable size, which we decoded to determine the types of the exchanged packets. More specifically, synchronization and acknowledgment packets were exchanged in both directions, while the Uplink (UL) stream from the HMD to the rendering server also contained frequent and relatively small head-tracking information packets. Naturally, the Downlink (DL) stream also had regular video frame packet bursts.

Fig. 1 is a visual representation of a short period of bidirectional VR streaming, showing the main data streams in both DL and UL. As the figure clearly shows, most of the traffic is concentrated in DL and consists of packet bursts encoding video frames. Video frame fragments were consistently found to be 1320 B long in all acquired traces, with a data size (the UDP payload) of 1278 B.

First, we considered the head tracking packets in the UL, which were all 192 B long. The distribution of the inter-packet interval Δ_u is shown in Fig. 2: tracking packets are relatively frequent, with a median interval of about 7 ms, but the distribution has a long tail. This suggests that head-tracking packets are usually sent at regular intervals, but some are transmitted adaptively if there were significant
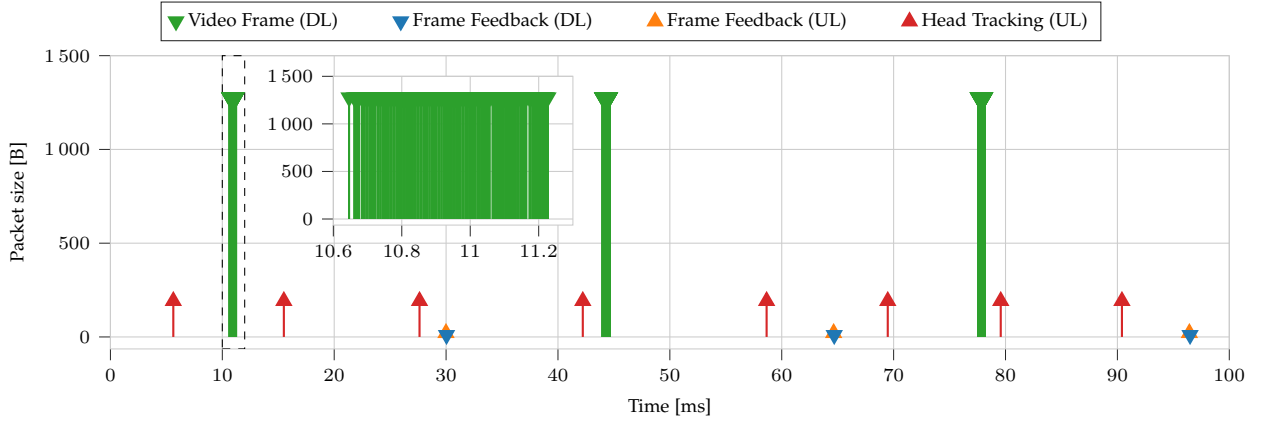
Fig. 1: Portion of traffic trace from *Virus Popper* (50 Mb/s, 30 FPS). In this trace, each video frame burst consists in about 130–140 individual fragments.
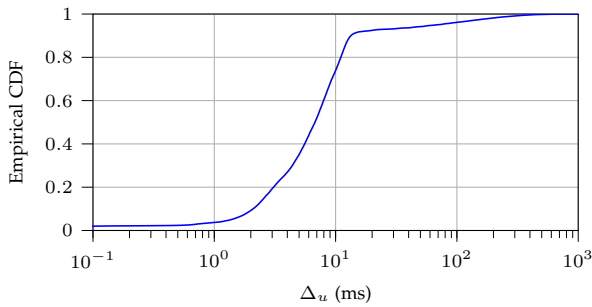

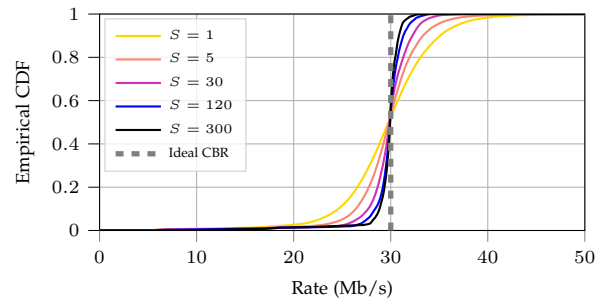Fig. 2: Head tracking packet inter-arrival time.

Fig. 3: Rate distribution for different MA window sizes S [number of frames].

headset movements that can affect the video rendering on the HMD. As we did not manage to decode the content of the tracking packets, a deeper analysis of their relation to head movements is left as future work.

By decoding the application protocol, we managed to identify frame boundaries and sort out the video data frames from metadata and control information. We can then consider the size of individual frames in a video trace. We note that non-video packets have a low impact on the total streaming data rate. Considering this, as well as the strong dependence of metadata on the application setup, we decided to focus mostly on the video frame data, discarding all other packets from our analysis. Our results can then be applied to any VR application using the same encoder.

The encoder uses the H.264 *Periodic Intra-Refresh* compression scheme to reduce the variation between frame sizes, so we do not expect a multimodal distribution, as would be the case for a classical keyframe-based encoding. As we mentioned above, encoding VR traffic as CBR offers a significant advantage for the network optimization, because frames of constant size make it possible for NS schemes to provide a guaranteed latency without wasting resources.

However, CBR encoding is not perfect, and frames may still have variable size, although the average rate almost perfectly matches the required one. We can use a simple Moving Average (MA) filter with a rectangular window S to examine the behavior of the traffic on longer timescales, which is useful if resource allocation is performed at a slower pace. Naturally, allocating resources every S frames

leads to a larger jitter between frames, but it can also improve the resource allocation efficiency, as size fluctuations tend to average out over multiple frames.

In order to measure this effect, we consider the *Virus Popper* trace, with a required rate $R = 30$ Mb/s and a $\varphi = 60$ FPS refresh rate. We only measure the video traffic, without packet headers and redundancy added by the application, which results in an average rate of 29.76 Mb/s. Fig. 3 shows the empirical Cumulative Distribution Function (CDF) of the rate, considering different values of the MA window sizes. If we consider each frame individually, there is a significant variation in the rate, which gradually reduces as we increase the number of frames over which the rate is measured.

However, providing reliable service will require a significant overhead even if we relax the slicing time: Fig. 4 shows the overflow rate, i.e., the difference between the actual rate and the expected 30 Mb/s CBR rate, as a function of the MA window sizes. The plot shows the standard deviation, as well as the 95th and 99th percentile overflow rates. If our aim is to provide 99% reliability, we need to overprovision by more than 8 Mb/s (i.e., almost 30% of the CBR rate) even if we consider a timescale of 100 ms for resource allocation, i.e., 6 frames. Even averaging over periods of multiple seconds leads to worst-case rates almost 4 Mb/s higher than the target, probably because of highly dynamic content in the video. Interestingly, the overflow standard deviation is approximately constant if the MA window
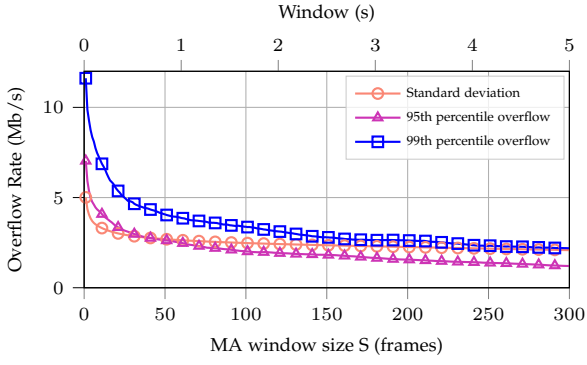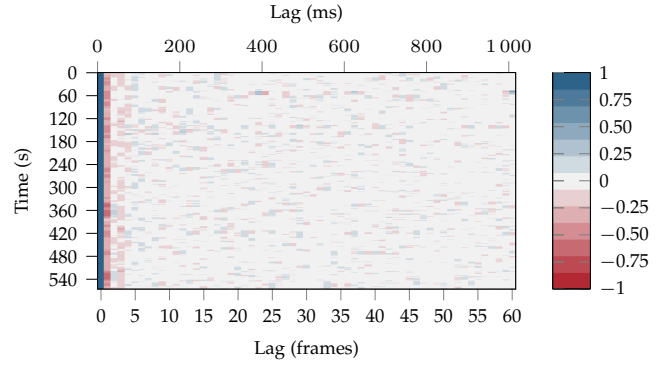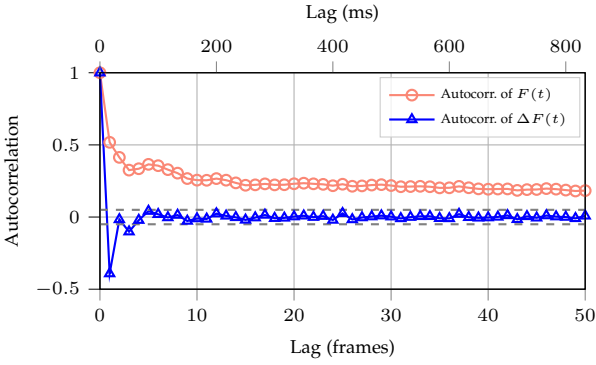
Fig. 4: Overflow rate for a target CBR of 30 Mb/s.

Fig. 6: Rolling windowed ΔF autocorrelation for *Virus Popper* (30 Mb/s, 60 FPS). The windows were 600 frames (10 s) long, with a time shift of 60 frames (1 s).

Fig. 5: Video frame size autocorrelation for *Virus Popper* (30 Mb/s, 60 FPS).

is longer than 50 frames, while the higher percentiles of the overflow continue to decay: this suggests that higher throughput periods tend to be shorter and more frequent, while there are longer periods of time with a bit rate below the average. Fig. 3 also hints at a skew in the distribution, as the left tail of the frame size empirical CDF is much longer.

Finally, we can analyze the autocorrelation of the frame size sequence $F(t)$, to identify patterns in how the sequence changes. Fig. 5 shows the autocorrelation of $F(t)$ and $\Delta F(t) = F(t) - F(t-1)$. While $F(t)$ has a strong long-term autocorrelation, due to the constant component, the $\Delta F(t)$ sequence has a strong negative autocorrelation between one frame and the next, while almost all longer time differences fall within the ± 0.05 range. This means that the encoder tends to balance out fluctuations between one frame and the next, such that a frame that is bigger than the previous one tends to be followed by a smaller one again. We can check that this holds throughout the whole video by computing a rolling window autocorrelation, shown in Fig. 6 for $\Delta F(t)$. In this case, the plot clearly shows that there are no strong long-term correlations in any part of the video. The frame difference sequence has a noticeable and consistent autocorrelation only with lags 1, 3, and 5, confirming the result from Fig. 5.

4.1 Frame Size Prediction

Let us consider the average size of future frames in the time interval $[t, t+T)$, given by

$$\overline{F_T}(t) = \frac{1}{T} \sum_{i=0}^{T-1} F(t+i). \quad (1)$$

We denote by $\hat{F}_T(t, \tau)$ an estimate of $\overline{F_T}(t + \tau)$, $\tau > 0$, i.e., considering a look-ahead of τ frames. We focus on linear predictors based on the last $N \geq 0$ samples, so that

$$\hat{F}_T(t, \tau) = \theta_0 + \sum_{j=1}^{N} \theta_j F(t - j + 1), \quad (2)$$

where $\boldsymbol{\theta} = [\theta_0, \ldots, \theta_N]$ is a weight vector, which determines the accuracy of the estimate. If $N = 0$, the estimate is just given by the parameter θ_0, and does not consider any past frames. The difference between actual and estimated value is captured by the error term $w(t, \tau, T) = \overline{F_T}(t + \tau) - \hat{F}_T(t, \tau)$, which will be denoted just as w in the following, for ease of writing. We can then consider two regression methods to determine the value of the parameter vector $\boldsymbol{\theta}$:

- *Ordinary Least Squares (OLS) linear regression*: least squares regression was independently developed by Gauss and Legendre in the 19th century [42], and is the most classic form of regression. In this case, the objective is to minimize the ℓ^2 norm of the sequence w. OLS regression can be useful in determining the average behavior of the underlying stochastic process, giving easily interpretable results on the quality of the prediction and the dynamics of the frame size over time;

- *Quantile regression* [43]: this technique estimates $\tilde{F}_T(t, \tau)$ so that the probability that it is higher than the real value, is not larger than p_s. This has obvious implications for network resource provisioning: as we are interested in providing enough resources to send a frame within the required latency with probability p_s, estimating the corresponding quantile might be the best way to get the required quality.

We also used *Robust linear regression* [44] to verify that the OLS prediction was not too sensitive to outliers. We considered a robust method using Huber's T norm instead of the
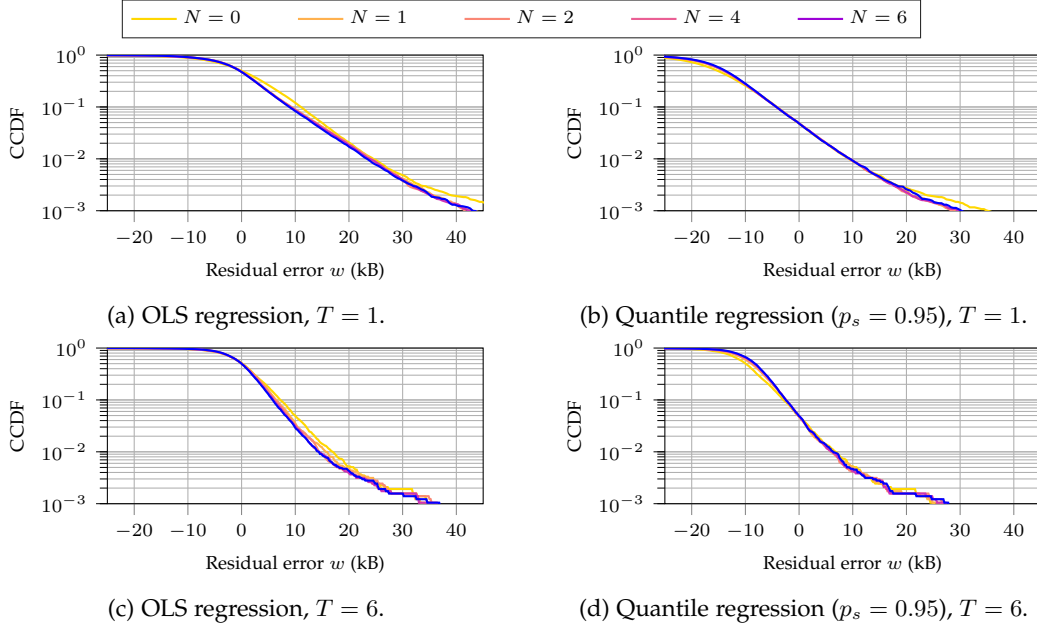
(a) OLS regression, $T = 1$.

(b) Quantile regression ($p_s = 0.95$), $T = 1$.

(c) OLS regression, $T = 6$.

(d) Quantile regression ($p_s = 0.95$), $T = 6$.

Fig. 7: Complementary CDF of the error w with $\tau = 1$ and different values of N and T.

ℓ^2 norm: the two norms have the same quadratic behavior if the error is smaller than a threshold δ, but Huber's T increases linearly for larger values. Setting the threshold to $\delta = \frac{\mathbb{E}[|F|]}{4}$, we found that the results matched exactly those of the OLS model, suggesting that outliers are not playing a relevant role in this case and thus letting us discard this model.

In this section, we will show results for both the OLS and the quantile regression models. As we stated above, while the results from OLS are more immediate, quantile regression is useful when focusing on scheduling network resources for a VR stream, which requires a model of the tail of the frame size distribution to provide latency guarantees.

We can now examine the results of the regression analysis for the *Virus Popper* trace, considering a rate of 30 Mb/s and 60 FPS. We focus on this video trace as the standard example in the paper, but other traces, even at different bit rates and frame rates, exhibit a similar behavior. Fig. 7 shows the complementary CDF of the residual error w, considering $\tau = 1$ and two different values of the averaging interval T. The first thing we can notice is that the error distribution has a slightly different shape for the OLS and quantile regression models, indicating that the difference in the two models is not simply a shift in the value of the intercept θ_0, but instead the two predictions are inherently different. We can also notice that there is some benefit from having a longer memory, although increasing N yields diminishing returns in terms of increased accuracy. Finally, we can confirm that the reliable transmission of this VR content will require significant overprovisioning, even when using prediction: for $T = 1$ the 95th percentile error of the OLS prediction is approximately 15 kB higher than the mean with any of the models, i.e., about 25% of the average frame size (which is 62.5 kB for this trace). In fact, this is close to the difference between the average predictions of the OLS and the quantile models.

This difference is about halved for $T = 6$, due to the fact that computing the average over multiple frames allows errors to compensate and cancel each other out. However, provisioning over multiple frames means that only the average amount of resources will be assigned to the stream, which will cause larger frames to have a higher latency, thus causing additional queuing delay to subsequent frames. Since the frame cannot be properly shown on screen until it is fully received, this translates to a higher jitter and reduces the QoE perceived by the user, making a lower value of T preferable.

Another fundamental component in evaluating the quality of a predictor is the autocorrelation of the residual error w: if the autocorrelation between subsequent samples of the residual error is high, the model did not capture some effect, usually due to an insufficient memory, i.e., too low a value of N. Fig. 8 shows the autocorrelation of w for different values of N: it is easy to see that models with $N < 4$, and particularly with $N = 0$ and $N = 1$, do not have enough memory to capture the frame size dynamics. This is more evident in quantile regression, which shows a higher autocorrelation for these models.

Finally, we can examine the effect of N and τ on the quality of the prediction by looking at Fig. 9, which shows the standard deviation of the residual error w as a function of these two parameters with $T = 1$. The figure clearly shows that increasing the memory of the model improves the prediction, but gives diminishing returns, as the difference between $N = 6$ and $N = 10$ is minimal. Furthermore, we see an expected increase of the error if τ increases, but this is not monotonic for $N < 3$: this might be due to the autocorrelation we observed in the w sequence, as $N < 3$ is not sufficient to fully represent the state of the stochastic process, resulting in suboptimal predictions.

4.2 Residual Error Characterization

We can then analyze the residual error w in more detail: as Fig. 10 shows, we attempted to fit the residual error on the
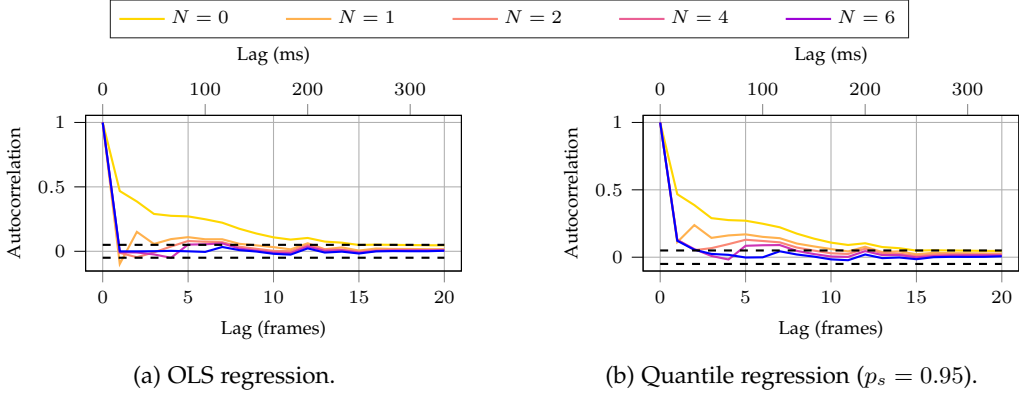
(a) OLS regression.

(b) Quantile regression ($p_s = 0.95$).

Fig. 8: Autocorrelation of the residual error w for next-frame prediction ($T = 1$, $\tau = 1$) for different values of N.
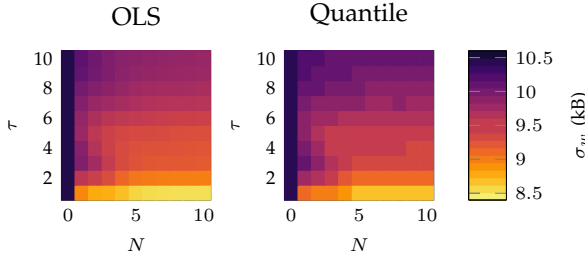

Fig. 9: Heatmap of the residual error standard deviation (measured in kB) as a function of N and τ, with $T = 1$.
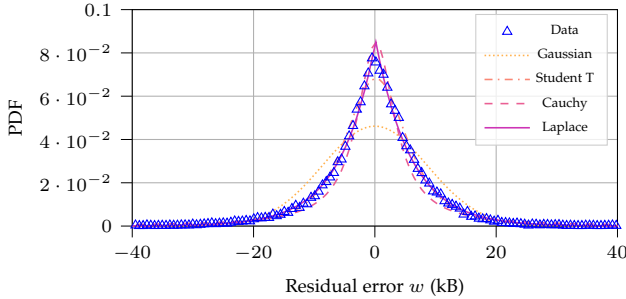

Fig. 10: Residual error after OLS prediction for *Virus Popper* (30 Mb/s, 60 FPS), with $T = 1$, $\tau = 1$, and $N = 6$.

frame size to various common bilateral distributions, and the maximum likelihood fit was given by the Laplace(μ, b) distribution, whose Probability Density Function (PDF) is given by:

$$p_w(x; \mu, b) = \frac{1}{2b} e^{-\frac{|x-\mu|}{b}}, \qquad (3)$$

where μ is the location parameter and b is the shape parameter. The same result held for all other traces in the dataset, leading us to infer that this distribution depends on some inherent property of the encoder and the way it generates frames, instead of specific features in the video content.

If we consider the residual error of the OLS regression method, the best estimate of the parameter μ is $\hat{\mu} = 0$, as having a non zero-mean residual error would imply a bias in the OLS estimator. The maximum likelihood estimator of

the shape parameter b is then given in [45] by:

$$\hat{b} = \frac{1}{N} \sum_{i=1}^{N} |x_i - \hat{\mu}|. \qquad (4)$$

The instantaneous value $\hat{b}_T(t, \tau)$ can then be determined from the model. As we are considering a regression model, in which previous frame sizes affect the distribution of future frames, we can simply perform an OLS regression on the absolute value of the residual error $|w|$ to find $\hat{b}_T(t, \tau)$. We can then represent the future frame size as a value $\hat{F}_T(t, \tau)$ given by the prediction plus a noise term w, whose distribution is Laplace($\hat{F}_T(t, \tau), \hat{b}_T(t, \tau)$). Interestingly, if we adopt this model, we have the complete distribution of the frame size, making it extremely easy to derive the quantile values for any desired point and considerably reducing the computational impact with respect to multiple quantile regressions. The quantile function $P^{-1}(p_s | T, \tau, t)$ is given by:

$$P^{-1}(p_s | T, \tau, t) = \hat{F}_T(t, \tau) + \hat{b}_T(t, \tau) \log(\min(2p_s, 2 - 2p_s)). \qquad (5)$$

4.3 Model Generalization

In the above, we studied how well regression models can predict future frame sizes $\hat{F}_T(t, \tau)$, but we always found the parameter vector $\boldsymbol{\theta}$ based on the same video trace. In the following, we study how prediction models perform when the regression is performed over multiple traces, with different bit rates and types of content. This has significant advantages, as finding a predictor for each specific video content requires acquiring traces for each content and quality level, while generalizing the predictor would allow for simpler deployment.

We consider $N = 6$ and $\tau = 1$, as we determined that $N = 6$ is sufficient to capture the dynamics of the model. In order to directly compare traces with different bit rates R and frame rates φ, we normalize the video traces by the expected frame size $\varphi^{-1} R$, obtaining a normalized parameter vector $\tilde{\boldsymbol{\theta}}$, which, given the linearity of our models, can be converted back to the original parameter vector in (1) as $\boldsymbol{\theta} = \frac{R\tilde{\boldsymbol{\theta}}}{\varphi}$. By normalizing our frame sizes, we can train and use our models on multiple traces with different values of R and φ. We then consider three generalized models:

(a) OLS regression, $T = 1$.

(b) Quantile regression ($p_s = 0.95$), $T = 1$.

(c) OLS regression, $T = 6$.
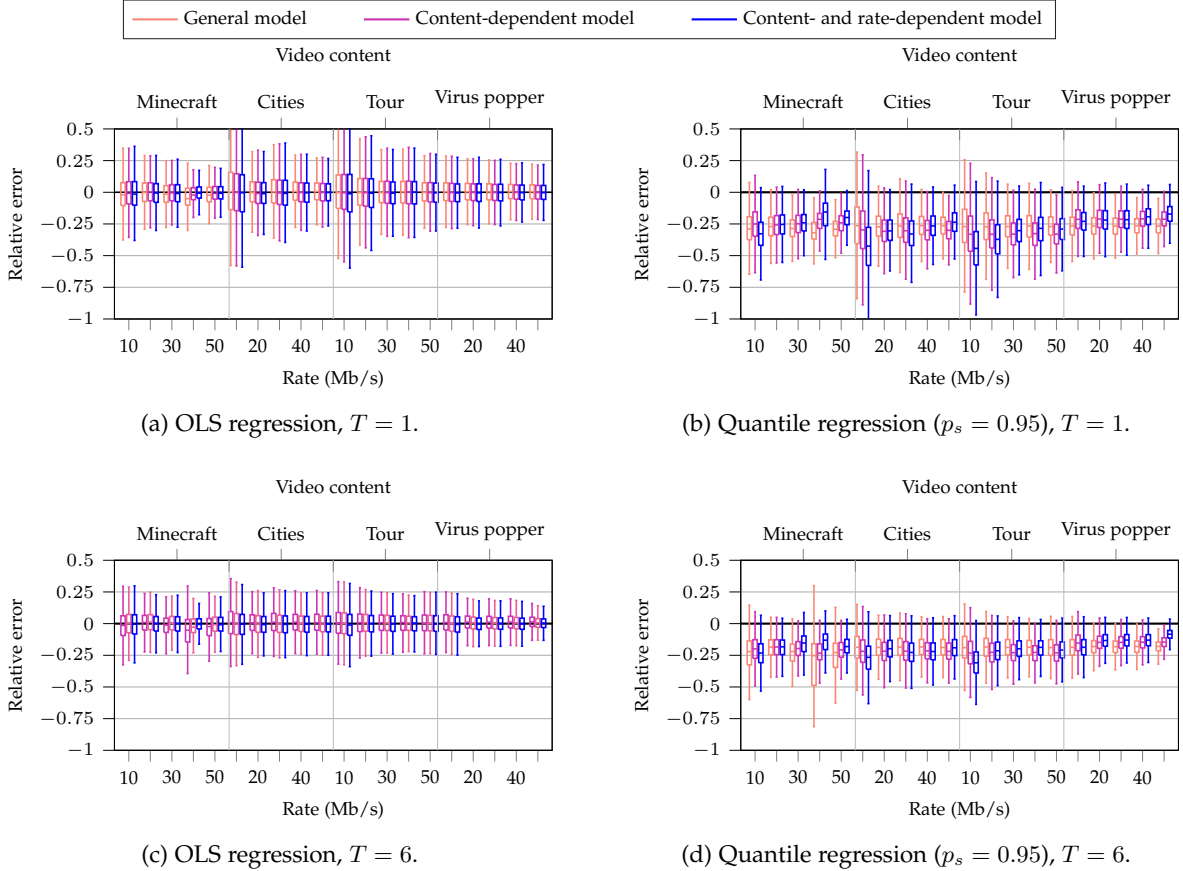

(d) Quantile regression ($p_s = 0.95$), $T = 6$.

Fig. 11: Boxplot of the relative residual error $\frac{\varphi w}{R}$ for different levels of generalization with $N = 6$ and $\tau = 1$. The traces are grouped by video content, and each group of boxplots shows the error at different bit rates for that video content.

1) A *general* model (GM), which computes $\boldsymbol{\theta}$ using the whole dataset, with different frame rates, bit rates, and video content types;
2) A *content-dependent* model (CM), which computes $\boldsymbol{\theta}$ using a single type of content (e.g., the *Virus Popper* game), but with different bit rates and frame rates;
3) A *content- and rate-dependent* model (CRM), which derives the parameter vector on a per-content, frame rate, and bit rate basis, i.e., a single trace.

Given that different values of R and φ can have different scales of errors which can be difficult to compare directly, in Fig. 11 we show the error normalized to the expected frame size R/φ. As the figure shows, the model can generalize quite well: the performance of CM is almost always similar to that obtained by CRM, making generalization across different bit rates and frame rates possible for the same video content. On the other hand, GM performs slightly worse, and has a large error in the Minecraft trace with $R = 40$ Mb/s: it is possible that this trace involves different dynamics in the content or head movements, leading to sharp differences even with other traces with the same type of content. On the other hand, GM has similar performance to CM and CRM with the OLS predictor, but shows a less consistent behavior for the quantile regressor. For example, the *Minecraft* trace with $R = 40$ Mb/s shows very different performance between the three models and different values of T. Furthermore, the *Virus Popper* trace seems to have a

smaller tail, as GM is more conservative than the models based only on that video content.

As we can see, using the quantile model leads to a prediction between 25% and 40% higher than the average, skewing the error distribution. We should also further highlight that averaging over multiple frames can also significantly reduce the error across almost all traces.

5 PREDICTIVE NETWORK SLICING

In this section, we consider an NS use case for the models we developed in Sec. 4. We assume that a number M of VR clients are assigned to a high-priority slice, with the objective of allowing each frame to be delivered before the generation of the next one, i.e., maintaining a latency below $1/60^{\text{th}}$ of a second. Provisioning the time and frequency resources for VR is a critical component of Beyond 5G networks, and guaranteeing limited latency while reducing the impact on other users is an important application of our model. Each client m then has a different bit rate R_m and, potentially, a different application, but we assume that the clients all share the same frame rate φ. Furthermore, each client m has a different spectral efficiency η_m, depending on its connection's Signal-to-Noise Ratio (SNR): users closer to the base station will have a stronger signal, and consequently, a higher transmission efficiency.

With a small loss of generality, we assume that clients are synchronized, i.e., frames are generated at the same time.

The orchestration can be adapted relatively easily to the more general case, but the notation would be much more cumbersome, and we maintain this simplifying assumption for the sake of readability. We can then assume that the network slicing orchestrator is equipped with the general frame size distribution model from Sec. 4.3, and can estimate the frame size distribution for arbitrary values of T and τ for each client m. We consider an orchestrator that can make decisions on the resource allocation only at times $t = kS$, $k \in \mathbb{Z}$, i.e., every S frames or, conversely, every $\Delta t = \frac{S}{\varphi}$ ms. In the following, we consider queued bits from earlier frames in the slicing as well. At time $t = kS$, we consider that the previous slice might have been unable to send all the data in time, leaving in the queue $q_m(t)$ bits that have to be sent in the following frame intervals.

5.1 Motion-To-Photon Latency

We can now analyze the MTP latency by dividing it into 6 components, which are shown in Fig. 12:

1) The movement of the user needs to be recorded and transmitted. For simplicity, we can assume head tracking packets to be transmitted at a constant interval Δ_u; in this case, the time between the motion and its transmission is $\tau_m \sim \mathcal{U}(0, \Delta_u)$.

2) The head tracking packet needs to be transmitted to the Cloud VR server. Considering that the uplink traffic is very light, as the packet is small, we can assume that it only incurs a constant propagation delay τ_p. We can also assume that Δ_u includes the uplink transmission time to the Base Station (BS), simplifying the model. In general, the transmission time from the HMD to the BS should be extremely low.

3) The head tracking data is received by the Cloud server, which then needs to produce a frame. The frame generation delay is $\tau_f \sim \mathcal{U}(0, \varphi^{-1})$.

4) The server needs to generate, render, and encode the frame. We denote this delay as τ_r, and assume that it is constant across short periods of time.

5) The frame is transmitted to the BS through a series of fiber optic links. As the capacity of fiber optic links is much higher than the Radio Access Network (RAN)'s, we can assume this to take only the propagation time τ_p.

6) The frame is transmitted from the BS to the HMD. This component depends on both the frame size and the downlink bandwidth allocated to its slice by the orchestrator.

If we set a maximum allowed MTP latency $T_{\max}$, we can then derive a condition on the minimum bandwidth $B(k)$ to be assigned to the n-th customer in the k-th interval of time:

$$B(k) \geq \frac{F(k)}{\eta \left(T_{\max} - \tau_m - 2\tau_p - \tau_f - \tau_r\right)}. \qquad (6)$$

where η is the spectral efficiency, known to the BS. However, τ_m and τ_f are random variables, so we can set a stricter condition that guarantees that the latency requirement is
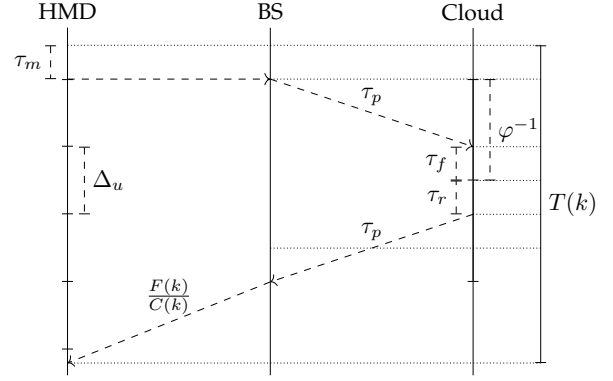

Fig. 12: Schematic of the components of the MTP latency.

met in the worst case by substituting their maximum values, i.e., Δ_u and φ^{-1}, respectively. We hence obtain

$$B(k) \geq \frac{F(k)}{\eta \left(T_{\max} - \Delta_u - 2\tau_p - \varphi^{-1} - \tau_r\right)}. \qquad (7)$$

For the sake of readability, we denote the maximum time allowed for the RAN transmission to fulfill the MTP latency requirement as T_{tx}, i.e.,

$$T_{\mathrm{tx}} = T_{\max} - \Delta_u - 2\tau_p - \varphi^{-1} - \tau_r. \qquad (8)$$

Finally, to ensure the stability of the queue at the BS, the average allocated bit rate, $\eta\mathbb{E}[B(k)]$, must be larger than the mean offered traffic, i.e.,

$$\eta\mathbb{E}[B(k)] > \varphi\mathbb{E}[F(k)]. \qquad (9)$$

5.2 Slicing schemes

We can then define four ways of allocating resources to the VR users:

1) *Individual FDMA (IF)*: each individual VR user is allocated to a different slice that it can fully exploit, and each slice has a constant bandwidth over the next S frames. The bandwidth is then given by:

$$B_{\mathrm{IF}}^{(m)}(kS + \ell) = \frac{P_m^{-1}(p_s|S, 1, kS) + \frac{q_m(t)}{S}}{\eta_m T_{\mathrm{tx}}}, \quad (10)$$

with $\ell \in \{1, \dots, S\}$. The scheme uses Frequency Division Multiple Access (FDMA), as the bandwidth B is constant over the whole slicing interval. In order to avoid instability, the $q_m(t)$ queued bits need to be considered in the slicing, but they are spread out over the S frames in the slicing period, so as to avoid excessive overprovisioning.

2) *Individual OFDMA (IO)*: in this case, each user is still assigned to their own individual slice, but there is a finer-grained control over the assignment of bandwidth resources, allowing frame-by-frame control of the bandwidth assignment by using Orthogonal Frequency Division Multiple Access (OFDMA). In this case, the queued bits can be handled in the first frame:

$$B_{\mathrm{IO}}^{(m)}(kS + 1) = \frac{P_m^{-1}(p_s|1, 1, kS) + q_m(t)}{\eta_m T_{\mathrm{tx}}}. \quad (11)$$

In all subsequent frames, i.e., for $\ell \in \{2, \ldots, S\}$, the bandwidth assignment $B_{\text{IF}}^{(m)}(t)$ is then given by:

$$B_{\text{IO}}^{(m)}(kS + \ell) = \frac{P_m^{-1}(p_s|1, \ell, kS)}{\eta_m T_{\text{tx}}}. \qquad (12)$$

3) *Aggregated FDMA (AF)*: while the two schemes described above give each user a slice of their own, this scheme performs FDMA, so it maintains a constant bandwidth throughout, but considers a single slice for the VR service. This allows users with larger than expected frames to exploit the bandwidth left unused by others with smaller than expected frames, but requires another, more fine-grained scheduler to divide the resources among users, which we will describe below. If we consider an oracle prediction, the required bandwidth $B^*(kS)$ to deliver all the generated data is given by:

$$B^*(kS) = \sum_{m=1}^{M} \frac{\frac{q_m(t)}{S} + \sum_{\ell=1}^{S} F^{(m)}(kS + \ell)}{\eta_m T_{\text{tx}}}. \qquad (13)$$

We can split the required bandwidth in two components:

$$B^*(kS) = B_q^*(kS) + B_f^*(kS), \qquad (14)$$

where we have:

$$B_q^*(kS) = \sum_{m=1}^{M} \frac{q_m(t)}{S \eta_m T_{\text{tx}}}; \qquad (15)$$

$$B_f^*(kS) = \sum_{m=1}^{M} \sum_{\ell=1}^{S} \frac{F^{(m)}(kS + \ell)}{\eta_m T_{\text{tx}}}. \qquad (16)$$

While $B_q^*(kS)$ is a deterministic, known value, as it only depends on the amount of queued bytes for each user, the bandwidth $B_f^*(kS)$ required to transmit future frames is unknown, as the size of these frames is stochastic. The distribution of $B_f^*(kS)$ is given by the convolution of MS Laplace distributions, and the details of its computation are given in the Appendix. If we denote the quantile function of this distribution as $P_{1,\ldots,M}^{-1}(p_s|S, 1, t)$, we get, with $\ell \in \{1, \ldots, S\}$:

$$B_{\text{AF}}(kS + \ell) = \frac{P_{1,\ldots,M}^{-1}(p_s|S, 1, kS) + \sum_{m=1}^{M} \frac{q_m(t)}{S}}{\eta_m T_{\text{tx}}}. \qquad (17)$$

We assume that users are synchronized, so that frames arrive approximately at the same time: this results in a need-based scheduler delivering the frames from all users approximately at the same time, allocating more bandwidth to users with a larger frame (or a lower spectral efficiency). This is a slight simplification, but we can easily adapt the mechanism for the asynchronous case with limited loss of performance. The choice of a need-based scheduler leaves the decision of setting user rates to flow admission, serving users equitably once they access the system.

4) *Aggregated OFDMA (AO)*: as we did for the individual slicing, we can also create aggregated slices with a finer-grained control of the bandwidth allocation.

In the first frame, the queues need to be flushed before new data can be transmitted:

$$B_{\text{AF}}(kS + 1) = \frac{P_{1,\ldots,M}^{-1}(p_s|1, 1, kS) + \sum_{m=1}^{M} q_m(t)}{\eta_m T_{\text{tx}}}. \qquad (18)$$

For $\ell \in \{2, \ldots, S\}$, we then have:

$$B_{\text{AO}}(kS + \ell) = \frac{P_{1,\ldots,M}^{-1}(p_s|1, \ell, kS)}{\eta_m T_{\text{tx}}}. \qquad (19)$$

Naturally, if there is only one user, i.e., $M = 1$, the AF and AO slicing schemes are the same as the IF and IO, respectively. In the same way, the FDMA and OFDMA slicing schemes are equivalent if $S = 1$, as the allocation is performed over the shortest possible unit of time, i.e., a single frame period. All slicing schemes ensure the stability of the queue by considering $q_m(t)$ in the bandwidth allocation, inherently ensuring that the condition in (9) is met. The calculation of the aggregated traffic distribution is given in the Appendix.

6 SIMULATION RESULTS

In the following, we run a simulation on a system implementing the slicing schemes we described in the previous section, analyzing the two fundamental Key Performance Indicators (KPIs) of the system: the MTP latency and the bandwidth B reserved to the VR users. Ideally, a system should be able to maintain the MTP latency below the required threshold while limiting the required bandwidth. The main parameters of the scenario are listed in Table 1, and will be used in all simulations, unless stated otherwise. We chose $T_{\max} = 50$ ms, which is consistent with the relevant literature, though looser than in the IEEE standard: as the application we used for the measuring has $\Delta_u = 7$ ms (on average) and $\varphi = 60$ FPS, even an instantaneous transmission would incur an MTP latency over 20 ms in the worst case. The stricter deadline set by the IEEE standard is then impossible to reach with the considered application, and we chose a looser but still realistic deadline, leaving the fulfillment of the more demanding one to future work with more powerful XR applications.

We also considered $\tau_p = 5$ ms and $\tau_r = 5$ ms, considering a powerful Cloud VR server located relatively close to the user. The final parameters are close to the 3GPP recommendation [30], which recommends a rate $R = 30$ Mb/s and $\varphi = 60$ FPS, although our DL latency budget is slightly looser, as the BS has 11.3 ms to stream each frame, while 3GPP specifies 10 ms as the target.

6.1 Single User

We can now examine the simulation results for a single user. As we remarked in the previous section, the IO scheme can reduce the jitter by having a more fine-grained prediction, as each frame will be allocated enough resources to be transmitted with probability p_s. On the other hand, the IF scheme has a rougher prediction, with consequently higher jitter, but will waste fewer network resources, as it can allow larger frames to be compensated by smaller ones before and after them. Both models are realistic, as they work under different assumptions: in the first case, the resources
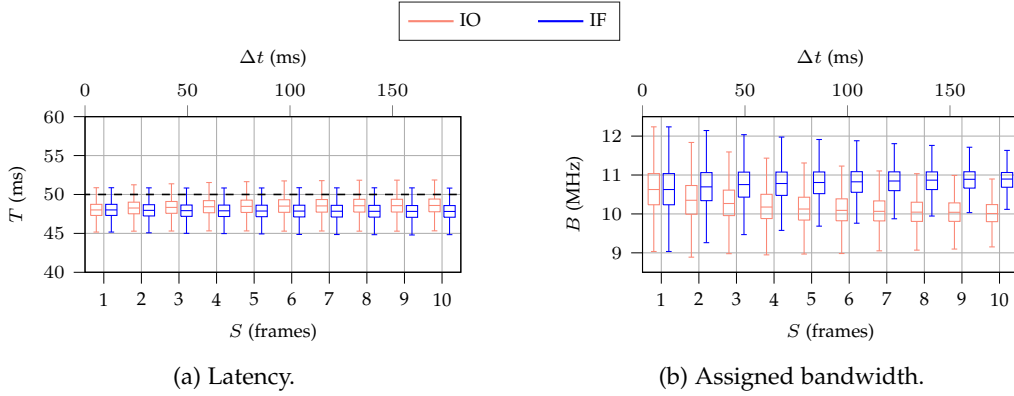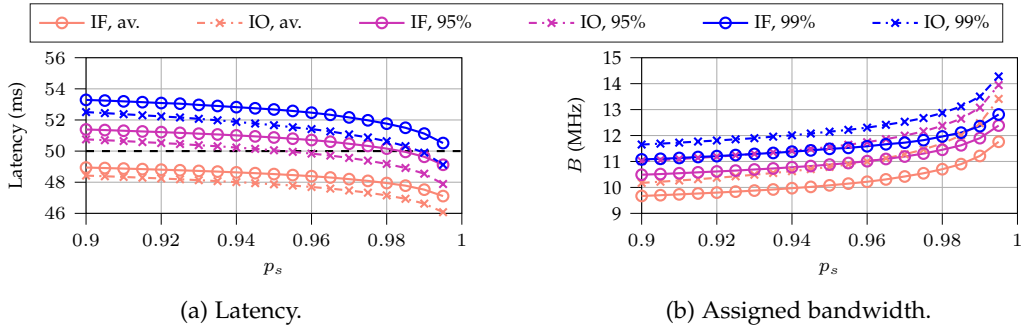
(a) Latency.

(b) Assigned bandwidth.

Fig. 13: Boxplot of slicing performance for IF and IO for a single user.

(a) Latency.

(b) Assigned bandwidth.

Fig. 14: Average and worst-case percentiles of the latency and assigned bandwidth of a single user as a function of the quantile p_s.

that are allocated for each frame need to be over both time and frequency, while the second case gives the slice a constant bandwidth over the slicing interval, which is the most common slicing model in the literature.

We can then look at the slicing schemes' performance as a function of S, setting $p_s = 0.95$ and $N = 6$: Fig. 13 shows boxplots of the latency and assigned bandwidth for IF and IO. Fig. 13a clearly shows that, while the slicing granularity has a limited effect on IO, the lower precision of IF means that the longer the slicing interval, the higher the average latency, and the worst-case latency, represented by the upper whisker of the boxplots, increases even more. On the other hand, as Fig. 13b shows, the bandwidth required by IF decreases as S grows, while the average bandwidth required by the IO algorithm remains roughly constant irrespective of the value of S, but always higher than the bandwidth used by IF.

TABLE 1: Basic scenario parameters.

Parameter	Value
$T_{\max}$	50 ms
Δ_u	7 ms
τ_p	5 ms
τ_r	5 ms
p_s	0.95
S	6 frames
N	6 frames
τ	1 frame
R	30 Mb/s
φ	60 FPS
Video content	Virus Popper

This behavior is to be expected, as the errors in frame prediction can compensate over a longer window, but comes at the cost of a higher latency. Naturally, the choice between the two models depends not only on the desired point in the trade-off between QoS and resource efficiency, but also on the capabilities of the underlying system: state-of-the-art slicing frameworks often consider a period $\Delta t = 100$ ms, which would correspond to $S = 6$ frames, and the granularity of the slicing over time and frequency will dictate whether IO is even an option.

It is also possible to simply increase the value of $C(t)$, e.g., by increasing p_s, in the IF scheme to match the IO performance in terms of latency, but IF will always be less efficient for the same latency target. Fig. 14 shows the slicing performance as a function of the value of p_s. Naturally, a higher p_s means a more conservative prediction of getting larger frames, which reduces the latency but increases the bandwidth requirements. The closer we get to 1, the more increasing p_s affects the latency, with a correspondingly larger increase in the bandwidth that is reserved to the VR flow. We can also notice that IF requires a much higher value of p_s to get the same performance as IO in terms of latency. A sensible example is to target a latency of one inter-frame interval, i.e., $\varphi^{-1} = 16.67$ ms (the dashed line in Fig. 14a), with a probability of 0.95 (the pink lines in Fig. 14). We notice that to meet this requirement, a value of $p_s \geq 0.96$ has to be chosen for the IO scheme, but the same requirement can only be fulfilled if $p_s \geq 0.99$ using IF. This corresponds to an average assigned bandwidth of at least 7.5 MHz for IO, but 7.64 MHz for IF. While the difference is
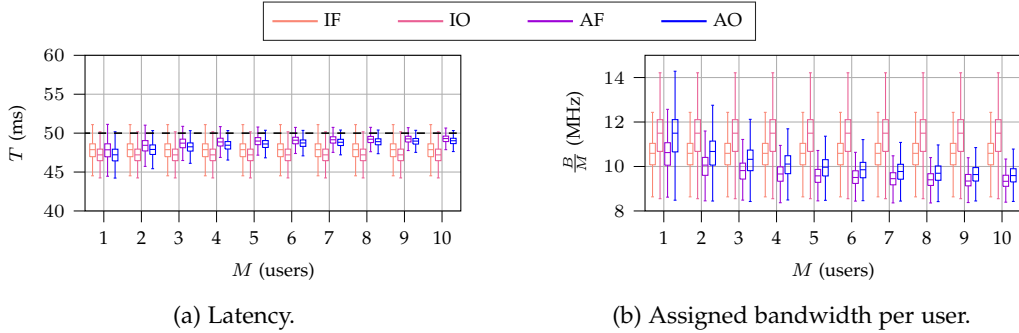
(a) Latency.

(b) Assigned bandwidth per user.

Fig. 15: Boxplot of the latency and per-user bandwidth as a function of the number of users.
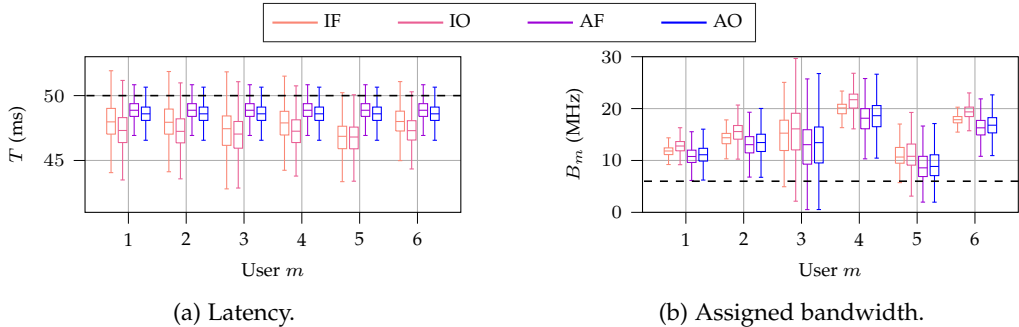

(a) Latency.

(b) Assigned bandwidth.

Fig. 16: Boxplot of the latency and bandwidth for each user.

not very significant, and the IF scheme can be used without a big performance loss, choosing the correct value of p_s to compensate for the slicing scheme's optimism is not simple, particularly in more complex network scenarios, while it is relatively straightforward for IO.

6.2 Multiple Users

We can now consider a more complex scenario, in which multiple VR users are served by the same BS. The first thing we need to understand is the impact of an increased number of users on the latency and allocation of resources. In this case, we will set up a scenario in which all users have the same spectral efficiency $\eta = 5\,\text{b/s/Hz}$, and stream the same content (i.e., the *Virus popper* trace at 60 FPS and 30 Mb/s), although starting with a random offset. This is to ensure that the scenario is as uniform as possible, and the only variable is the number M of users in the system. Furthermore, as we stated in Sec. 5.2, we assume that all VR users are synchronized, i.e., frames from all users come at the same time: this is a slight simplification, which does not have a significant effect on performance.

Fig. 15 shows the latency and assigned bandwidth for the scenario: if we look at the latency boxplot in Fig. 15a, we can note that the average latency for the two aggregated schemes increases with M, but the higher percentiles actually decrease as M increases: this is because, as aggregating more users leads to errors in the frame size prediction compensating each other, the resource allocation can be more precise, aiming at satisfying the φ^{-1} latency requirement, but not trying to go far below that. As the number of users grows, the distribution of the latency will tend towards deterministically achieving φ^{-1} with limited jitter. This is a significant advantage with respect to individual slicing,

which is compounded by the lower resource use, as Fig. 15b shows: as the number of users increases, the bandwidth allocated to each user remains the same for individual slicing schemes, while the aggregate schemes can reduce the total amount of resources. As for the latency, this is because independent variations in the frame size compensate each other, leading to a lower overall uncertainty on the total frame size and a better resource provisioning. Finally, as for the single user case, using OFDMA can slightly reduce the latency, overshooting the deadline less often, but at the cost of a higher resource utilization: the same error compensation effect that we mentioned across different users can be exploited over different frames, at the cost of a higher latency violation probability.

We then analyze the per-user results more in depth by considering a scenario with $M = 6$ users, whose detailed parameters are given in Table 2: each user has a different video bit rate R_m and a different spectral efficiency, but they have a common frame rate φ and are synchronized. As we did above, we consider a predictive slicing orchestrator using the general model obtained by performing the regression over all traces. The videos also have a random offsets, so even users with the same content have independent

TABLE 2: Multi-user scenario parameters.

User m	VR content	R_m (Mb/s)	η_m (b/s/Hz)	$\bar{B}_m (MHz)$
1	Virus Popper	10	1.5	6.67
2	Cities	20	2.5	8
3	Minecraft	30	3	10
4	Tour	40	3.5	11.43
5	Minecraft	50	5.5	9.09
6	Virus Popper	40	4	10

(a) Latency (IF and IO).

(b) Latency (AF and AO).
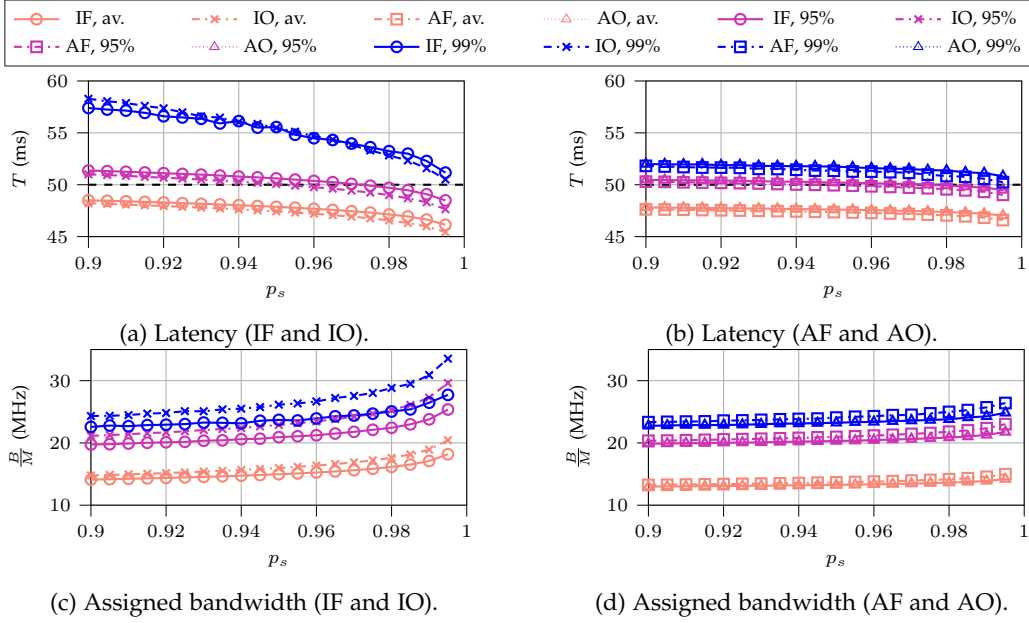
(c) Assigned bandwidth (IF and IO).

(d) Assigned bandwidth (AF and AO).

Fig. 17: Average and worst-case percentiles of the latency and assigned bandwidth as a function of the quantile p_s.

(a) 95th percentile.
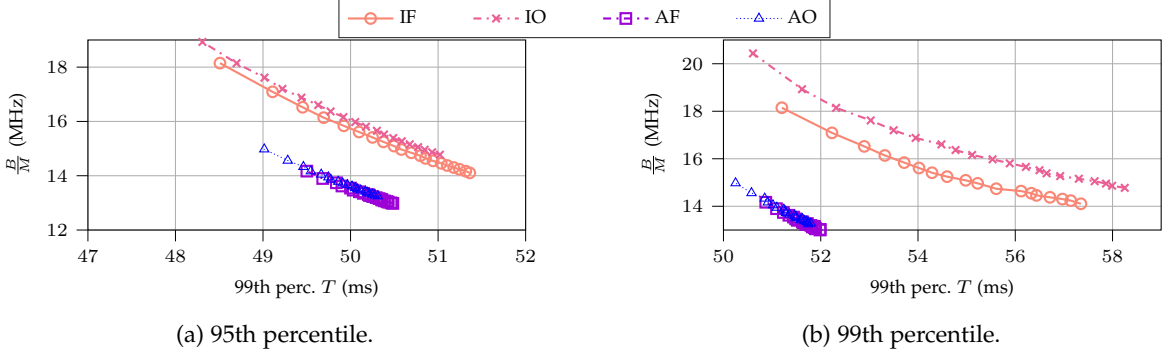
(b) 99th percentile.

Fig. 18: Pareto curves for the performance of the slicing schemes.

traces. Fig. 16 shows the latency and assigned bandwidth for the 6 users, presenting some interesting patterns. As Fig. 16a shows, the latency for all users is the same when using the aggregated slicing schemes: this is an effect of using a need-based scheduler when allocating resources inside the slice. On the other hand, latency is different when using individual slicing, with users 5 and 6 having a lower latency violation probability. On the other hand, the bandwidth assigned to each user, shown in Fig. 16b, is similar for all schemes, with the aggregated ones having a slightly lower resource utilization. This is due to the fact that the average required bandwidth $\bar{B}_m = \frac{R_m}{\eta_m}$, whose value for each user is given in Table 2, is the main factor in assigning bandwidth resources, both with individual and aggregated schemes: we can easily see that users 1, 2, and 5, who have the lowest values of $\bar{B}_m$, are also assigned the least bandwidth by the slicing schemes. Interestingly, user 5 is actually the one with the lowest bandwidth, although users 1 and 2 have lower values of $\bar{B}_m$: this is due to the higher relative variations in the video traces at lower bit rates, as can be easily seen from Fig. 11, so that in order to meet the $p_s = 0.95$ requirement, the slicing schemes have to overprovision more for those users.

We can also look at the performance as a function of p_s in the scenario given in Table 2, as we did for the single-user case. The results are shown in Fig. 17: it is easy to see that aggregated schemes manage to maintain a much lower latency in the worst case with a lower total bandwidth, as the individual schemes have either a latency higher than the 50 ms threshold (for lower values of p_s) or a far higher resource utilization (for higher values of p_s). Interestingly, the performance difference between FDMA and OFDMA is negligible for the aggregated schemes: the prediction errors of a user are effectively compensated by the other users, enhancing the overall performance.

We can further analyze the performance difference between the schemes by plotting their Pareto curves. Pareto curves are useful to show two-dimensional performance metrics which need to be traded against one another: the curve includes all points at the edge of the achievable performance region, i.e., points for which it is impossible to improve one metric without making the other worse. In our case, the two metrics are the MTP latency and the bandwidth: ideally, we would like both to be as low as possible, and the Pareto curve is another way of showing the trade-off we discussed above.

If we define the performance of a slicing scheme g in terms of latency and bandwidth as $q_g(p_s) = (T, B)$, we can say that p_s *dominates* p'_s, and we write $p_s \succ p'_s$ where p_s has a better performance for both metrics, i.e.,

$$T(g, p_s) < T(g, p'_s) \wedge B(g, p_s) < B(g, p'_s). \tag{20}$$

We can then define the Pareto curve $\mathcal{P}_g$ as the set of points that are not dominated by any other point:

$$\mathcal{P}_g \triangleq \{q_g(p_s), \forall p_s \mid \nexists p'_s : p'_s \succ p_s\}. \tag{21}$$

Fig. 18 shows the Pareto curves for the 4 schemes, considering $p_s \in [0.9, 0.995]$. The two plots show the performance in terms of the average assigned bandwidth per user and the 95th and 99th percentiles of latency, and confirm our analysis: the aggregated schemes can significantly outperform the individual ones, with a bandwidth reduction of more than 10% to obtain the same latency performance at the 95th percentile and more than 20% at the 99th percentile. We can also note that, while the difference between IF and IO is relatively small for the 95th percentile, it grows for the 99th percentile, as taking the worst case highlights the limits of the FDMA approach. On the other hand, the difference between AF and AO is negligible. In addition to significantly improving the performance, choosing an aggregated scheme is also computationally simpler, as the slicing algorithm will only need to allocate resources to a single VR slice and not to each individual user.

7 CONCLUSIONS

This work aims at closing a gap in the literature on traffic source modeling: there are several analyses for passive streaming, both 2D and in immersive setups with Head Mounted Devices (HMDs), and some for live gaming traffic in 2D, but none for interactive VR with strict latency requirements and *quasi*-CBR encoding. We analyzed live captures from a setup we devised, publishing both the dataset and the code for the analysis, and presented the performance of two regression models. The first part of our discussion analyzes the prediction models, determining the necessary memory in the linear regression, the residual distribution, and the correctness of the linear model. The prediction models are simple and flexible, as they generalize extremely well across different traces and bit rate settings: this means that a shared pre-trained model can be used with good performance across different video content types and bit rate levels.

We then showed a simple Network Slicing (NS) scenario, which highlights the importance of the trade-off between resource efficiency and QoE. This is a first step towards fully designing an NS system able to satisfy the stringent QoS requirements of XR applications also in critical scenarios, e.g., in industrial settings, in which the consequences of network failures are not only discomfort and nausea for the user, but also significant delays in production and even safety hazards. The results we obtained show a significant trade-off between resource efficiency and MTP latency guarantees, which can be improved significantly if multiple VR users are put together in the same slice, sharing Radio Access Network (RAN) resources using a fair scheduler.

There are several additional analyses and opportunities for future work, that can be divided in two main directions. The first potential avenue of research is a wider characterization, with different encoding parameters and even different encoders, and considering different applications, going beyond simple VR games to include the industrial and commercial use cases we mentioned above, and a wider set of subjects. The traces should also integrate a record of the head movements of the users, as they correspond to shifts in the point of view of the VR headset and are expected to be strongly correlated with frame size changes.

The other challenge is to actually design slicing schemes and scheduling algorithms able to take into account the nature of the traffic and accommodate it, efficiently exploiting the prediction and adapting to the peculiarities of different communication technologies or even multiple independent links. The use of packet-level coding to protect the stream from link failures and deep fading events, can be promising avenues to design a solid framework to support XR in mission-critical scenarios. The study of these techniques at all levels of the communication stack, simulating connection impairments in repeatable conditions through a full-stack network simulator, is our first priority in the ongoing work on this subject.

APPENDIX
Aggregated traffic distribution

Given that the frame size distribution for a single user is known and well defined, we can derive the distribution of the total required bandwidth $B_f^*(k)$ for the M users in closed form. In the following, we will consider the case in which $S = 1$, but the calculation can be trivially extended to the case with $S > 1$. Specifically, the bandwidth required to deliver the next frame for all the M users is defined in Eq. (16) as a weighted sum of Laplace random variable:

$$B_f^*(k) = \sum_{m=1}^{M} \eta_m^{-1} F^{(m)}(k). \tag{22}$$

In the following, we omit the index k for the sake of readability. The user spectral efficiencies η_m^{-1} are constant scalars which result in a scaling of the frame size distribution, i.e.,

$$B_m = \eta_m^{-1} F^{(m)} \sim \text{Laplace}\left(\alpha_m, \beta_m\right), \tag{23}$$

where $\alpha_m = \frac{\mu_m}{\eta_m}$ and $\beta_m = \frac{b_m}{\eta_m}$. The distribution of the sum of independent random variables is obtained as the convolution of the corresponding PDFs, denoted by $p_m(x)$. In the Laplace transform domain, this translates to a product of the transforms of the densities. Given that the Laplace transform $\mathcal{L}[\cdot]$ of the Laplace distribution is

$$\mathcal{L}\left[p_m(x)\right](s) = \mathcal{L}\left(\frac{1}{2\beta_m} e^{-\frac{|x - \alpha_m|}{\beta_m}}, s\right)$$
$$= e^{-\alpha_m s} \frac{1}{1 - \beta_m^2 s^2}, \tag{24}$$

the transform of the PDF $p(x)$ of the sum $B_f^*(k)$ is

$$\mathcal{L}\left[p(x)\right](s) = e^{-s \sum_{m=1}^{M} \alpha_m} \prod_{m=1}^{M} \frac{1}{1 - \beta_m^2 s^2}. \tag{25}$$

In the case when the poles have multiplicity equal to 1, the product can be represented with its partial function decomposition as

$$
\begin{aligned}
\mathcal{L}\left[p(x)\right](s) &= e^{-s\sum_{m=1}^{M}\alpha_m} \prod_{m=1}^{M} \frac{1}{1-\beta_m^2 s^2} \\
&= e^{-s\sum_{m=1}^{M}\alpha_m} \sum_{m=1}^{M} \frac{\gamma_m}{1-\beta_m^2 s^2},
\end{aligned}
\tag{26}
$$

where the values of γ_m can be obtained through the residue (or Heaviside cover-up) method, and are equal to

$$
\gamma_m = \frac{\beta_m^{2(M-1)}}{\prod_{n\neq m}\left(\beta_m^2 - \beta_n^2\right)}.
\tag{27}
$$

Thanks to the additive and the shift property of the Laplace transform, we get the PDF of

$$
\begin{aligned}
p\left(x - \sum_{m=1}^{M}\alpha_m\right) &= \mathcal{L}^{-1}\left[\mathcal{L}\left[p(x)\right](s)\right]\left(x - \sum_{m=1}^{M}\alpha_m\right) \\
&= \sum_{m=1}^{M} \frac{\beta_m^{2(M-1)-1} e^{-\frac{|x|}{\beta_m}}}{2\prod_{n\neq m}\left(\beta_m^2 - \beta_n^2\right)}.
\end{aligned}
\tag{28}
$$

We can then use this result to directly compute the quantile function $P_{1,\dots,M}^{-1}(p_s|1,1,k)$. Extending the result to larger values of S and multiple frames, we can simply plug in the function to obtain the AF and AO slicing schemes.

The above calculation is correct in the case of simple poles. We can then briefly discuss the more general case of repeated poles. Repeated poles can be present in Eq. (25) if the distributions of the bandwidth required by different users have the same shape parameter β (i.e., the ratio between the shape parameter b_m and the user spectral efficiency η_m), regardless of the mean α. This may be the case when the same or similar applications are streamed to multiple, possibly static users in the same room, e.g., in the case of a VR arena. Thus, the distribution of the frame sizes, determined by the application, and the spectral efficiencies, determined by the propagation environment, may be the same for different users. Namely, we can consider the most general case when there are $P \leq M$ unique poles $\{\beta_1, \beta_2, \dots, \beta_P\}$ of order $\{p_1, p_2, \dots, p_P\}$, $\sum_{i=1}^{P} p_i = M$, i.e., the users are grouped in P clusters with similar β values.

In this case, the partial fraction representation is more involved than that in Eq. (26). Taking into account the repeated poles, the product in Eq. (26) can be rewritten as

$$
\prod_{m=1}^{M} \frac{1}{1-\beta_m^2 s^2} = \prod_{i=1}^{P} \frac{1}{\left(1-\beta_i^2 s^2\right)^{p_i}},
\tag{29}
$$

and can thus be decomposed as

$$
\prod_{i=1}^{P} \frac{1}{\left(1-\beta_i^2 s^2\right)^{p_i}} = \sum_{h=1}^{P}\sum_{k=1}^{p_h} \frac{\gamma_{h,k}}{\left(1-\beta_h^2 s^2\right)^k} = f(s).
\tag{30}
$$

Several methods exist for determining the γ vector. The residue method offers a general solution:

$$
\gamma_{h,k} = \operatorname{Res}\left(g_{h,k}, \beta_h^2\right),
\tag{31}
$$

where $\operatorname{Res}(g_{h,k}, \cdot)$ is the residue of the function

$$
g_{h,k}(s) = \left(1 - \beta_h^2 s^2\right)^{k-1} f(s),
\tag{32}
$$

and can be computed as

$$
\begin{aligned}
&\operatorname{Res}\left(g_{h,k}, \beta_h^2\right) = \\
&= \frac{1}{(p_h - k)!}\left[\frac{\mathrm{d}^{p_h-k}}{\mathrm{d}(s^2)^{p_h-k}}\left(1 - \beta_h^2 s^2\right)^{p_h} f(s)\right]_{s^2 = \beta_h^2}.
\end{aligned}
\tag{33}
$$

REFERENCES

[1] Huawei Technologies Co., "Empowering consumer-focused immersive VR and AR experiences with mobile broadband," Huawei Technologies Co., White Paper, 2016, accessed on May 2022. [Online]. Available: https://www.huawei.com/en/industry-insights/outlook/mobile-broadband/insights-reports/vr-and-ar

[2] ——, "AR insight and application practice," Huawei Technologies Co., White Paper, 2021, accessed on May 2022. [Online]. Available: https://carrier.huawei.com/~/media/CNBGV2/download/bws2021/ar-insight-and-application-practice-white-paper-en.pdf

[3] Oculus Business, "Virtual reality – Set to enter the business mainstream," Oculus Business, White paper, Sep. 2020, accessed on May 2022. [Online]. Available: https://go.facebookinc.com/security-whitepaper.html

[4] Qualcomm Technologies, "The mobile future of eXtended Reality (XR)," Qualcomm Technologies, Presentation, Nov. 2020, accessed on May 2022. [Online]. Available: https://www.qualcomm.com/media/documents/files/the-mobile-future-of-extended-reality-xr.pdf

[5] 3GPP, "Extended Reality (XR) in 5G," 3GPP, Technical Report (TR) 26.928, Dec. 2020.

[6] ITU-T, "Requirements for mobile edge computing enabled content delivery networks," ITU, Report F.743.10, Nov. 2019.

[7] H. G. Kim, W. J. Baddar, H.-T. Lim, H. Jeong, and Y. M. Ro, "Measurement of exceptional motion in VR video contents for VR sickness assessment using deep convolutional autoencoder," in *ACM Symposium on Virtual Reality Software and Technology (VRST)*, Gothenburg, Sweden, Nov. 2017.

[8] A. A. Barakabitze, A. Ahmad, R. Mijumbi, and A. Hines, "5G network slicing using SDN and NFV: A survey of taxonomy, architectures and future challenges," *Computer Networks*, vol. 167, p. 106984, Feb. 2020.

[9] Nokia, "Cloud gaming and 5G – Realizing the opportunity," Nokia, White Paper, 2020. [Online]. Available: https://onestore.nokia.com/asset/207843

[10] Huawei, "Preparing for a Cloud AR/VR future," Huawei, White Paper, 2017, accessed on May 2022. [Online]. Available: https://www-file.huawei.com/-/media/corporate/pdf/x-lab/cloud_vr_ar_white_paper_en.pdf?la=en

[11] M. Lecci, A. Zanella, and M. Zorzi, "An ns-3 implementation of a bursty traffic framework for virtual reality sources," in *ACM Workshop on ns-3 (WNS3)*, Virtual Conference, US, Jun. 2021.

[12] M. Lecci, M. Drago, A. Zanella, and M. Zorzi, "An open framework for analyzing and modeling XR network traffic," *IEEE Access*, vol. 9, pp. 129 782–129 795, Sept. 2021.

[13] M. Lecci, F. Chiariotti, M. Drago, A. Zanella, and M. Zorzi, "Temporal characterization of XR traffic with application to predictive network slicing," in *IEEE International Symposium on a World of Wireless, Mobile and Multimedia Networks (WoWMoM)*, Belfast, UK, Jun. 2022.

[14] J. Latta and D. Oberg, "A conceptual virtual reality model," *IEEE Computer Graphics and Applications*, vol. 14, no. 1, pp. 23–29, Jan. 1994.

[15] "IEEE Standard for Head-Mounted Display (HMD)-Based Virtual Reality(VR) Sickness Reduction Technology," *IEEE Std 3079-2020*, pp. 1–74, 2021.

[16] M.-W. Seo, S.-W. Choi, S.-L. Lee, E.-Y. Oh, J.-S. Baek, and S.-J. Kang, "Photosensor-based latency measurement system for head-mounted displays," *Sensors*, vol. 17, no. 5, May 2017.

[17] A. Blate, M. Whitton, M. Singh, G. Welch, A. State, T. Whitted, and H. Fuchs, "Implementation and evaluation of a 50 kHz, 28μs motion-to-pose latency head tracking instrument," *IEEE Transactions on Visualization and Computer Graphics*, vol. 25, no. 5, pp. 1970–1980, May 2019.

[18] J.-P. Stauffert, F. Niebling, and M. E. Latoschik, "Simultaneous run-time measurement of motion-to-photon latency and latency jitter," in *IEEE Conference on Virtual Reality and 3D User Interfaces (VR)*, Mar. 2020, pp. 636–644.

[19] J. Zhao, R. S. Allison, M. Vinnikov, and S. Jennings, "Estimating the motion-to-photon latency in head mounted displays," in *IEEE Virtual Reality (VR)*, Los Angeles, California, Mar. 2017, pp. 313–314.

[20] S.-W. Choi, S. Lee, M.-W. Seo, and S.-J. Kang, "Time sequential motion-to-photon latency measurement system for virtual reality head-mounted displays," *Electronics*, vol. 7, no. 9, Sept. 2018.

[21] S. Tanwir and H. Perros, "A survey of VBR video traffic models," *IEEE Communications Surveys & Tutorials*, vol. 15, no. 4, pp. 1778–1802, Jan. 2013.

[22] S. Liew and D.-Y. Tse, "A control-theoretic approach to adapting VBR compressed video for transport over a CBR communications channel," *IEEE/ACM Transactions on Networking*, vol. 6, no. 1, pp. 42–55, Feb. 1998.

[23] N. Mohsenian, R. Rajagopalan, and C. A. Gonzales, "Single-pass constant- and variable-bit-rate MPEG-2 video compression," *IBM J. Res. Dev*, vol. 43, no. 4, pp. 489–509, Jul. 1999.

[24] M. Carrascosa and B. Bellalta, "Cloud-gaming: Analysis of Google Stadia traffic," in *arXiv*, Sep. 2020. [Online]. Available: https://arxiv.org/pdf/2009.09786.pdf

[25] A. Di Domenico, G. Perna, M. Trevisan, L. Vassio, and D. Giordano, "A network analysis on Cloud Gaming: Stadia, GeForce Now and PSNow," *Network*, vol. 1, no. 3, pp. 247–260, Oct. 2021.

[26] P. Graff, X. Marchal, T. Cholez, S. Tuffin, B. Mathieu, and O. Festor, "An analysis of Cloud Gaming platforms behavior under different network constraints," in *International Conference on Network and Service Management (CNSM)*, Virtual Conference, Oct. 2021.

[27] O. S. Peñaherrera-Pulla, C. Baena, S. Fortes, E. Baena, and R. Barco, "Measuring Key Quality Indicators in Cloud Gaming: Framework and assessment over wireless networks," *Sensors*, vol. 21, no. 4, Feb. 2021.

[28] B. Hentschel, M. Wolter, and T. Kuhlen, "Virtual Reality-based multi-view visualization of time-dependent simulation data," in *IEEE Virtual Reality Conference*, Lafayette, LA, USA, Mar. 2009, pp. 253–254.

[29] F. Chiariotti, "A survey on 360-degree video: Coding, quality of experience and streaming," *Computer Communications*, vol. 177, pp. 133–155, Sep. 2021.

[30] 3GPP, "Study on XR (Extended Reality) Evaluations for NR," 3GPP, Technical Report (TR) 38.838, Dec. 2021.

[31] V. Sciancalepore, K. Samdanis, X. Costa-Perez, D. Bega, M. Gramaglia, and A. Banchs, "Mobile traffic forecasting for maximizing 5G network slicing resource utilization," in *IEEE Conference on Computer Communications (INFOCOM)*, Atlanta, GA, USA, Apr. 2017.

[32] C. Marquez, M. Gramaglia, M. Fiore, A. Banchs, and X. Costa-Perez, "Resource sharing efficiency in network slicing," *IEEE Transactions on Network and Service Management*, vol. 16, no. 3, pp. 909–923, Jun. 2019.

[33] H. Jiang, T. Wang, and S. Wang, "Multi-scale hierarchical resource management for wireless network virtualization," *IEEE Transactions on Cognitive Communications and Networking*, vol. 4, no. 4, pp. 919–928, Oct. 2018.

[34] L. Tang, X. He, X. Yang, Y. Wei, X. Wang, and Q. Chen, "ARMA-prediction-based online adaptive dynamic resource allocation in wireless virtualized network," *IEEE Access*, vol. 7, pp. 130 438–130 450, Sep. 2019.

[35] C. Gutterman, E. Grinshpun, S. Sharma, and G. Zussman, "RAN resource usage prediction for a 5G slice broker," in *International Symposium on Mobile Ad Hoc Networking and Computing (MobiHoc)*, Catania, Italy, Jul. 2019, pp. 231–240.

[36] N. Van Huynh, D. T. Hoang, D. N. Nguyen, and E. Dutkiewicz, "Real-time network slicing with uncertain demand: A deep learning approach," in *IEEE International Conference on Communications (ICC)*, Shanghai, China, May 2019, pp. 1–6.

[37] A. Arfaoui, R. El-Azouzi, M. Haddad, and E. Sabir, "Flexible network slicing assisted 5G for video streaming with effective and efficient isolation," in *IEEE International Teletraffic Congress (ITC 32)*, Osaka, Japan, Sep. 2020, pp. 156–164.

[38] M. Chen, W. Saad, and C. Yin, "Virtual Reality over wireless networks: Quality-of-Service model and learning-based resource management," *IEEE Transactions on Communications*, vol. 66, no. 11, pp. 5621–5635, Nov. 2018.

[39] M. Chen, W. Saad, C. Yin, and M. Debbah, "Data correlation-aware resource management in wireless Virtual Reality (VR): An echo state transfer learning approach," *IEEE Trans. on Communications*, vol. 67, no. 6, pp. 4267–4280, Jun. 2019.

[40] X. Yang, Z. Chen, K. Li, Y. Sun, N. Liu, W. Xie, and Y. Zhao, "Communication-constrained mobile edge computing systems for wireless virtual reality: Scheduling and tradeoff," *IEEE Access*, vol. 6, pp. 16 665–16 677, Mar. 2018.

[41] Nvidia, "Video Codec SDK Documentation," 2021. [Online]. Available: https://docs.nvidia.com/video-technologies/video-codec-sdk/nvenc-video-encoder-api-prog-guide/

[42] S. M. Stigler, "Gauss and the invention of least squares," *The Annals of Statistics*, pp. 465–474, May 1981.

[43] R. Koenker and G. Bassett Jr, "Regression quantiles," *Econometrica: journal of the Econometric Society*, pp. 33–50, Jan. 1978.

[44] C. Yu and W. Yao, "Robust linear regression: A review and comparison," *Communications in Statistics-Simulation and Computation*, vol. 46, no. 8, pp. 6261–6282, Sep. 2017.

[45] R. M. Norton, "The double exponential distribution: Using calculus to find a maximum likelihood estimator," *The American Statistician*, vol. 38, no. 2, pp. 135–136, May 1984.